Differential permissivity of human cerebrovascular endothelial cells to enterovirus infection and specificities of enterovirus 71 in crossing an in vitro model of human blood brain barrier

Journal Item

Title

Differential permissivity of human cerebrovascular endothelial cells to enterovirus infection and specificities of enterovirus 71 in crossing an in vitro model of human blood brain barrier

Authors

Romain Volle[1,2], Christine Archimbaud[1,2], Pierre-Olivier Couraud[4], Ignacio A. Romero[5], Babette Weksler[6], Audrey Mirand[1,2], Bruno Pereira[3], Cécile Henquell[2], Hélène Peigue-Lafeuille[1,2], and Jean-Luc Bailly[1,2*]

Affiliations

1 Clermont Université, Université d'Auvergne, EPIE, EA 4843, Clermont-Ferrand, France

2 CHU Clermont-Ferrand, Service de Virologie, Clermont-Ferrand, France

[3] CHU Clermont-Ferrand, DRCI, Clermont-Ferrand, France

[4] Inserm, U1016, Institut Cochin, Paris, France

[5] Department of Life, Health and Chemical Sciences, Open University, Milton Keynes, U.K

[6] Weill Cornell Medical College, New York, NY, USA

Running title

Impairment of the blood brain barrier by enteroviruses

Word counts: Abstract, 203; Main text, 5429

Correspondent footnote: Jean-Luc Bailly

Phone: +33 4 73 17 81 42; Fax: +33 4 73 75 48 51; j-luc.bailly@udamail.fr

ABSTRACT

Human cerebral microvascular endothelial cells (hCMEC/D3 cell line) form a steady polarized barrier when cultured *in vitro* on a permeable membrane. Their susceptibility to enterovirus (EV) strains was analysed to investigate how these viruses may cross the blood-brain barrier. A sample of 88 virus strains was selected on phylogenetic features among 44 epidemiologically relevant types of the four EV species A–D. The EV-A71 genome was replicated at substantial rates while the infectious virus was released at extremely low but sustained rates at both barrier sides for at least 4 days. EV-A71 antigens were detected in a limited number of cells. The properties of the endothelial barrier (structure and permeability) remained intact throughout infection. The chronic EV-A71 infection was in sharp contrast with the productive infection of cytolytic EVs (**e.g.** echoviruses 6 and 30). The hCMEC/D3 barriers infected with the latter EVs exhibited elevated proportions of apoptotic and necrotic cells, which resulted in major injuries to the endothelial barriers with dramatic increase of paracellular permeability and virus crossing to the abluminal side. The following intracellular rearrangements were also seen: early destruction of the actin cytoskeleton, remodelling of intracellular membranes, and reorganization of the mitochondrion network in a small cluster near the perinuclear space.

INTRODUCTION

Enteroviruses (EVs; *Picornaviridae*) form a large group of non-enveloped enteric viruses, of which more than 100 different serotypes are human pathogens classified within four taxonomic species (EV-A to EV-D). Human EVs are transmitted through faecal-oral and respiratory routes and they actively replicate in the mucosa and epithelial cells of the throat and intestinal tract. Viral invasion of the intravascular space or viremia may result in spreading to sites such as the skin, heart and central nervous system (CNS).

The most common clinical manifestation associated with CNS EV infections is aseptic meningitis. Encephalitis, cerebellitis, myelitis, and poliomyelitis are also observed but less frequently (Khetsuriani *et al*., 2006; Antona *et al*., 2007). There is evidence for hematogenous and neural routes of poliovirus (PV) dissemination and both involve viremia (Sabin, 1956); the two routes are not mutually exclusive. By the neural pathway, it is suggested that the virus is conveyed by retrograde axonal transport from infected tissues to the CNS via peripheral nerves (Ren & Racaniello, 1992; Gromeier & Wimmer, 1998). In mouse models, PV can be transported along nerves through either a process involving the CD155 receptor or a receptor-independent manner (Okha *et al*., 2012). Investigations with different animal models have revealed a possible link between neurological injury caused by enterovirus A71 (EV-A71) and retrograde axonal transport of the virus to the CNS (Chen *et al*., 2007; Khong *et al*., 2012). The occurrence of encephalomyelitis and subsequent paralysis associated with these two EVs could be explained by transport via the neural pathway but the inefficiency of the axonal transport limits virus access to the CNS (Lancaster & Pfeiffer, 2010).

Alternatively, a virus in the bloodstream may enter the CNS by crossing the vascular endothelium in the meninges, the choroid plexus, or the brain parenchyma. PV-1 was suggested to cross the mouse blood-brain barrier (BBB) independently of the CD155 receptor and of infected leucocytes (Yang *et al*., 1997). During EV-A71 infection, viremia early after the onset

63 of disease was related to severe CNS involvement in young children (Cheng *et al*., 2014) and
64 to neurological impairment in experimentally infected rhesus monkeys (Zhang et al., 2011). In
65 neonates infected with coxsackievirus B3 (CV-B3), a high blood viral load was related to
66 greater disease severity (Yen *et al*., 2007). Using sensitive quantitative gene amplification
67 techniques to amplify viral RNA from the cerebrospinal fluid (CSF), it is possible to detect
68 evidence of EV infection of the CNS in patients with aseptic meningitis early after the onset of
69 disease in both children and adults (Volle et al., 2014). Our current knowledge about the
70 processes involved in EV immigration into the CSF is still limited. As this inflammatory
71 disease of the subarachnoid space is common to most EV serotypes, it is assumed that viruses
72 travel through the blood, breaching the blood-CSF barrier either directly or through infected
73 leukocytes. A number of studies showed that PV, CV-B3, and EV-A71 can infect various
74 immune cells (Eberle *et al*., 1995; Vuorinen *et al*., 1996; Haddad *et al*., 2004; Wahid *et al*.,
75 2005a; 2005b; Tabor-Godwin *et al*., 2010). These data suggest a role of infected leukocytes in
76 EV dissemination to the CNS through a "Trojan-horse" process. In vitro studies showed the
77 susceptibility to different EVs of human vascular endothelial cells of different tissue
78 origins (Conaldi *et al*., 1997; Ylipaasto *et al*., 2010; Saijets *et al*., 2003; Liang *et al*., 2004;
79 Zanone *et al*., 2003; Bozym *et al*., 2010). In addition, PV-1 and CV-B3 induce different cell
80 signalling and endocytosis pathways in human brain microvascular endothelial cells
81 (HBMEC), which is suggestive of possible variations in BBB crossing between EV types
82 (Bozym *et al*., 2010; Coyne *et al*., 2007).

83 In this study we used the human cerebral microvessel endothelial cell line D3
84 (hCMEC/D3) as a model of brain endothelium (Weksler *et al*., 2005; 2013). The hCMEC/D3
85 cells were used as a model for investigating whether or not EVs can breach an endothelial
86 barrier. We first examined the susceptibility of hCMEC/D3 cells to infection by a set of 44 EV
87 serotypes and then analysed the ability of a subset of EVs to cross endothelial barriers.
88

89 **RESULTS**

90 **Susceptibility of hCMEC/D3 cells to 44 EV types.** We used a first set of 88 virus strains
91 (**Table S1**) chosen within species B (EV-B; n=37 types), EV-A (n=5), EV-C (n=1), and EV-D
92 (n=1). Susceptibility of hCMEC/D3 cells to EV strains was assessed in duplicate at 24 h p.i.
93 by measurement of the production of viral RNA and infectious virus (**Fig. S1)**. The virus yield
94 exhibited a positive correlation (Spearman's rho 77%, p-value <0.001) with viral RNA
95 production **(Fig. 1a)**. The virus strains selected among the EV-B types displayed different
96 replication patterns defined by two arbitrarily selected thresholds of 0.00 $\log_{10}$ infectious
97 particles and 3.00 $\log_{10}$ genome copies per cell. The highest infectivity rates (from −0.55 to
98 2.86 $\log_{10}$ infectious particles per cell and 2.12 to 5.53 $\log_{10}$ genome copies per cell) were
99 determined for the epidemiologically infrequent types echovirus 1 (E-1) and EV-B69 and the
100 epidemic types E-6, E-11, E-12, E-13, and E-30. The strains selected among CV-B and EV-A
101 types displayed the lowest infectivity rates (respectively, from −2.89 to 0.01 and −2.38 to −0.41
102 $\log_{10}$ infectious particles per cell, and −0.44 to 3.53 and 2.01 to 4.51 $\log_{10}$ genome copies per
103 cell).

104 Kinetics of viral RNA production performed in triplicate for EV-A71, E-6, E-30, and
105 E-12 strains showed the highest rates of virus replication between 2 and 6 h p.i. (p-value 0.001;
106 **Fig. 1b)**. Different peaks of viral RNA production were reached at 24 h p.i. among the viruses
107 tested (mean±SD in $\log_{10}$ copies per cell): EV-A71 (3.29±0.58), E-30 (4.15±0.30), E-6
108 (5.30±0.25), and E-12 (5.56±0.21). These RNA levels were consistent with those obtained in
109 **Fig. 1a**: 2.46±0.63, 3.85±0.26, 5.02±0.15, and 5.46±0.15, respectively.

110 We determined the number of infected cells at 6 h p.i. (before extensive release of virus
111 progeny) to investigate whether the variations in susceptibility of hCMEC/D3 cells were
112 related to differences in the infection efficiencies of EV strains. The infected cells were
113 numbered in triplicate by computer-assisted image processing of low magnification

114 epifluorescence pictures. The highest proportion of infected cells (>30%) was determined for
115 E-19, EV-B69, and E-1, and intermediate proportions of 10–30% were obtained with E-12 and
116 E-16 (**Fig. 1c**). Less than 10% of infected cells were counted for virus strains of various types
117 (E-30, E-3, E-7, CV-B6, E-4, E-14, E-18, EV-A71, E-9, E-32, CV-B3, and E-25). About 20
118 infected cells per cm² were counted for E-27 and E-11, and only 3–5 infected cells per cm² for
119 EV-B70, EV-B77, CV-A9, E-15, E-24, and E-26 (data not shown). Two E-6 and E-13 strains
120 exhibited different infection efficiencies (E-6/CF2660-01 >30%; E-6/CF158061-11 and E-
121 13/CF1275-00 10–30%; E-13/CF1925-01 <10%). The overall data suggest variations in the
122 susceptibility of the hCMEC/D3 cells to infection by different EV types and subtypes.
123
124 **Cell mortality during virus infection and multidimensional analysis of EV infectivity.** The
125 mortality rates of infected hCMEC/D3 cells were determined in quadruplicate at 24 h p.i. for a
126 subset of 15 EV strains representative of different susceptibility patterns determined above in
127 hCMEC/D3 cells **(Fig. 1d)**. The mortality threshold was defined by the highest value of the
128 standard deviation calculated with mock infected cells (i.e. 10%). High cell mortality rates
129 >50% were found with E-1 and EV-B69, and cell death resulted from both necrosis and
130 apoptosis. Intermediate cell mortality rates between 40 to 50% were estimated for E-12, E-
131 6/CF2660-01, and E-30/CF282-97. Other virus strains of the two latter types caused lower cell
132 mortality (30–40%). Two E-13 strains were related to different cell mortality rates (CF1274-
133 00, 38.3%; CF1925-01, <30%). Mortality of cells infected with EV-A71 (11%) was similar to
134 that of mock infected cells.
135 We used principal component analysis (PCA) to visualize on a map the ordination of
136 the 15 EV strains according to the proportion of infected cells, the production of viral genomes,
137 the yield of infectious particle production, and cell mortality rates (**Fig. S2**). The proportion of
138 infected cells and cell mortality exhibited a positive correlation, hereafter designated cell

sensitivity (x-axis). The productions of viral genomes and infectious virus were positively correlated and designated as viral replication (y-axis). As cell sensitivity and viral replication were orthogonal, they were not correlated with each other. PCA confirmed that the hCMEC/D3 cell line displayed large differences in sensitivity to EV types and strains within the same type (**Fig. 2**). We selected viral strains representative of different PCA patterns for further investigations with endothelial barriers (Table S2).

Variations in permeability and structural integrity of endothelial barriers among EV types. We prepared endothelial barriers *in vitro* with the hCMEC/D3 cells (see **Fig. S3**) and quantified infection with five EV types so that infection and paracellular permeability were assessed in the same samples. The structural features of mock-infected endothelial monolayers and their restrictive permeability were analysed with transmission electron microscopy (TEM) and clearance of a non-permeable fluorescent compound (**Figs. S3 and S4**). Endothelial barriers infected with E-6, E-11, E-12, and E-30 strains exhibited little change in paracellular permeability at 24 h p.i. but permeability progressively increased afterwards (**Fig. 3a–3d**). A release of viral genomes (>6 $\log_{10}$ copies) was detected at 6 h p.i. at both barrier sides, but in the abluminal compartment, viruses were detectable below the titration threshold for E-12 and E-30. The release of infectious progeny reached highest levels at 24–48 h p.i. Scanning electron microscopy (SEM) allowed the identification of three main cytological alterations (**Fig. 4**). Compared to mock infected controls, which had the appearance of joined cobblestones (**Fig. 4a–4c**), the infected endothelial barriers exhibited cells with structural features suggestive of necrosis (damage plasma membrane) and apoptosis (preserved and budded plasma membrane), indicated, respectively, by red and green arrow heads in **Fig. 4d–4l**. Rounded cells without apparent altered plasma membrane were suggestive of early steps of cell death (see blue arrow heads). On the basis of these analyses, we found evidence of large amounts of altered cells,

which caused breaches within endothelial barriers, as indicated by the visualization of pores of the microporous membrane (white arrow heads).

The paracellular permeability of endothelial barriers infected with the EV-A71 strains (genogroups C1 and C2) was maintained at levels similar to those of mock-infected barriers until 96 h p.i. (**Fig. 3e and 3f**). The abluminal release of EV-A71 genomes and infectious virus was highest at 24 h p.i. and remained constant at slightly lower levels up to 96 h p.i. The infectious progeny was below the titration threshold at the abluminal side after 24 h p.i., but was consistently determined at low levels at the luminal side. SEM observations showed few groups of infected cells and a limited number of small breaches (**Fig. 4m–4o**).

Intracellular changes in endothelial barriers during EV infection. The endothelial barriers were analysed by TEM to visualize the intracellular features of infected hCMEC/D3 cells and to investigate variations between EV types. The altered cells of endothelial barriers infected with the E-6/CF2660-01 strain displayed features indicative of virus infection, which were similar to those caused by E-30 and E-12 (data not shown). At 24 h p.i., the impaired cells displayed shrunken nuclei relocated near the cell membrane and contained myriads of virus-induced vesicle-like membranous structures, 200 nm in diameter (**Fig. 5a and 5b**). These structures had either single or double membranes and were organized in extensive intracellular arrangements (**Fig. 5c**). Some infected cells showed evidence of tubular structures with positive membrane invagination that enclosed cytoplasmic components (**Fig. 5d**). Clusters of electron-dense granules between membranous structures were suggestive of viral particles (**Fig. 5e**). Mitochondria were grouped near the membranous structures, which contrasted with mock-infected cells, in which mitochondria formed an extensive network (**Fig. S4**). Large single-membrane vesicles (600–1000 nm in diameter) contained electron-dense cytoplasmic material and multilamellar structures resembling autophagic vacuoles (**Fig. 5c**).

189 In contrast to the features described above, the impaired cells of endothelial barriers
190 infected with EV-A71/CF166105-10 displayed a number of structural variations. As shown in
191 **Fig. 6a–6d**, the EV-A71 infected cells maintained an elongated shape and contained nuclei
192 similar in shape to those seen in control barriers. Remodelling of intracellular components
193 included vesicle-like structures and mitochondria clustered near the nucleus whereas EV-A71-
194 induced membranous structures had a uniform round shape with a diameter of 500 nm and a
195 multilamelar structure (**Fig. 6e–6i**).
196
197 **Intracellular injury patterns common to EV types.** The early virus-induced intracellular
198 injuries at 6 h p.i. were further analysed by confocal microscopy and viral replication was
199 detected by staining the VP1 protein. The infected cells displayed major reduction in staining
200 of polymerized actin in comparison to controls (**Fig. 7a–7r vs Fig. 7s–7u)**. This indicates
201 effective cytoskeleton impairment early after the initiation of viral protein synthesis and would
202 explain the subsequent cell rounding.
203 Early virus-induced changes in the mitochondrion network were analysed with a
204 fluorescent probe that accumulates in active mitochondria. Mitochondria were stained in all
205 virus-infected cells (**Fig. 8a–8o**) but, in contrast to mock-infected controls, they were clustered
206 in a perinuclear area (**Fig. 8p–8r**). Rearrangement of the mitochondrion network was marked
207 in cells exhibiting prominent staining of the VP1 protein at 6 h p.i. (see white arrowheads).
208 Cells with reduced VP1 staining exhibited no or minor changes in the mitochondrion network
209 (see yellow arrowheads). Mitochondrion clustering was dependent on viral replication
210 intensity but was not directly related to cell rounding, since cells that were not yet round were
211 also displaying clustered mitochondria.
212

DISCUSSION

Human EV infections are associated with meningitis, encephalitis, and encephalomyelitis but our current knowledge about CNS invasion by enteric viruses is still scant. The BBB may represent a common entry pathway for EVs during viremia, which precedes disease onset. In this study, we used the human cerebral microvascular endothelial cell line hCMEC/D3 as a model system for investigating EV entry routes into the CNS through the human BBB. We showed that the hCMEC/D3 cells were permissive to infection by a large array of EVs and found major differences between types and genogroups. Most EV strains occupied a central position in the susceptibility spectrum of hCMEC/D3 cells, notably the E-6, E-13, and E-30 strains, and intratypic variations may be related to individual genetic differences among genogroups and subgenogroups. A wide range of cellular receptors has been observed in human EVs (reviewed in Merilahti *et al*., 2012). Although we did not examine the binding processes of EVs to the hCMEC/D3 cell surface, there is a large body of earlier experimental evidence to suggest that the intertypic variations in hCMEC/D3 susceptibility to EVs can be attributed to their propensity for using a wide range of receptors and internalization processes (Ylipaasto *et al*., 2010; Coyne *et al*., 2007; Bozym *et al*., 2010). For instance, E-1 stands apart within the susceptibility spectrum of hCMEC/D3 cells to EV infection, a pattern which may be related to the fact that it is the only type known to bind integrin α2β1 (Bergelson *et al*., 1993). A number of EV types examined in our study (E-6, E-11, E-12, E-13, and E-30) bind the same cellular receptor CD55 (Bergelson *et al*., 1995). Yet, the virus strains of these types did not cluster in the same area of the susceptibility spectrum of hCMEC/D3 cells. This suggests that additional factors other than canonical receptors should be considered and that genogroup features may be involved.

Our investigation provides evidence of two major clusters among EV types. A first cluster consists of the EVs that exhibit a highly cytolytic phenotype, produce infectious

progeny, and induce extensive disruption of the endothelial barrier. Early during cellular infection by these viruses, the amount of virus genomes released in the abluminal compartment was >10,000 times higher than that of infectious progeny. We assumed that paracellular transport of viral RNA and defective virus particles was not involved because barrier permeability to the fluorescent reporter was not yet compromised at this time, a hypothesis that is also supported by SEM observations. At 24 h p.i., the difference between the release of viral genomes and virus particles was substantially reduced at the abluminal side as a result of the destruction of the endothelial barrier caused by infected dying cells. In contrast, the release of genomic material was relatively constant over time at the luminal sides. Accordingly, massive amounts of viral genomes appeared to drain off the cells through their basolateral membrane early during infection by a yet unknown process.

The second cluster comprises CV-B and EV-A71 types, which produced no impairment of the *in vitro* model of endothelium barrier. A key observation, in sharp contrast with the above data, is that hCMEC/D3 cells are moderately permissive to EV-A71 infection. This pattern resulted from a high replication rate of the viral genome but a remarkably poor production of infectious viruses. Both the virus and viral RNA were released from the luminal and basolateral sides of the endothelial barrier but at disproportionately different rates as the infectious virus was consistently detected at minute amounts. This process was maintained for at least 4 days and did not induce a breakdown of the barrier nor changed the paracellular permeability as measured with the LY surrogate marker. This non-disruptive pattern occurred even when the barriers were inoculated with a MOI of about 100 $TCID_{50}$ per cell (data not shown), which suggests that it was not dependent on the initial infection conditions but was more probably related to post-entry factors. A non-disruptive and long-term replication pattern was also shown for CV-B3 and CV-B5 (data not shown). A persistent replication was reported earlier for CV-B3 and CV-B4 in human dermal microvascular endothelial cells (Zanone *et al.*,

2003). A flavivirus West Nile virus can cross *in vitro* BBB models by infection of endothelial cells (Verma *et al*., 2009). The brain endothelium crossing and infection by West Nile virus is not related to direct disturbance of the endothelial barrier integrity *in vitro,* as observed in our study for EV-A71 and CV-B. The loss of BBB integrity associated with the West Nile virus may be related to up regulation of cell adhesion molecules (e.g. VCAM-I, E-Selectin) in infected endothelial cells, thus promoting trans endothelial migration of leucocytes *in vivo* (Verma *et al*., 2009; 2010).

The infected cells showed typical ultrastructural features of a picornavirus infection. We found evidence for both apoptosis and necrosis among infected cells regardless of the EV type, in agreement with data indicating a competition between cell death pathways and picornavirus replication (Agol & Gmyl, 2010). We also observed disruption of the actin cytoskeleton network and that of intercellular junctions as evidenced by the rounding of infected cells. The actin cytoskeleton has an important role in the maintenance of stable inter endothelial junctions and prevents paracellular transport to the brain (Stamatovic *et al*., 2012; Spindler & Hsu, 2012). Remodelling of intracellular membranes was the third hallmark of a picornavirus infection seen in infected hCMEC/D3 cells but discrete variations occurred between echoviruses (E-6, E-12, and E-30) and EV-A71. In the echovirus infections, we found evidence of single and double membrane vesicles organized in compact arrangements near the nucleus and of structures that displayed positive membrane invagination. Both features were reported earlier in Vero and Hela cells infected by CV-B3 and PV-1, respectively (Limpens *et al*., 2011; Belov *et al*., 2012). The vesicular structure in the EV-A71 infected hCMEC/D3 cells was characterised by less condensed vesicles and an increased proportion of multilamellar and large vesicles. Finally, our analyses with TEM and fluorescence microscopy showed clustering of the mitochondrion network, a previously unobserved feature of EV infections that occurred early during the virus infection and whose origin is still unclear. It may be related to virus-

induced disruption of microtubules, as suggested for cells infected with the hepatitis B virus (Kim *et al*., 2007). A similar feature was also reported for African swine fever virus, another DNA virus, and was related to coupling between viral translation and ATP synthesis (Rojo *et al*., 1998).

The most frequent EV infections of the CNS cause meningitis as a result of virus replication in the cells of the leptomeninges, the brain coverings (Rotbart, 1995). These infections are usually self-limited because the meninges are directly accessible to immunologic surveillance and subject to rapid immune responses (Engelhardt & Coisne, 2011). The varying amounts of viruses in the CSF of patients with EV meningitis within few hours after the onset of symptoms (Volle et al., 2014) may reflect virus unloading from these infected sites. The meningeal blood vessels, which form the barrier between blood and CSF, are only made of non-fenestrated endothelial cells; this contrasts with the BBB, which includes other cell types. Accordingly, our endothelium model is consistent with the blood-CSF barrier. The infection of endothelial cells reported in this study for a large array of EV types may occur during the earliest stages of viremia, which develops following EV replication in peripheral tissues. The local EV replication may contribute to infection of leptomeninges and development of a neuro-inflammatory disease. Of note, regional blood flow reduction and cerebral vasculitis can be observed in children with E-30 aseptic meningitis (Nishikawa et al., 2000). Care must be taken in making generalised conclusions of pathophysiology based on *in vitro* model systems and the transcellular passage for neural spread of EVs requires close examination in an appropriate in vivo model.

MATERIALS AND METHODS

Cell lines and viruses. HCMECs were grown in EBM-2 basal medium (Lonza) supplemented with 5% fetal bovine serum (FBS), 1% penicillin (10,000U), 1% streptomycin (10mg/ml; GE Healthcare Life Science), 1% chemically defined lipid concentrate (Invitrogen), 10 mM of HEPES, 1.4 µM of hydrocortisone (Sigma Aldrich), 1.5 $\mu g \times ml^{-1}$ of ascorbic acid (Sigma Aldrich), and 200 $ng \times ml^{-1}$ of basal fibroblast growth factor (Sigma Aldrich). The cells were seeded for all experiments on rat collagen I-coated culture surfaces (RD-System). The rabdomyosarcoma (RD) cells were grown in RPMI 1640 medium (Lonza) with 1% penicillin/streptomycin, and 4% FBS. The buccal epithelial carcinoma (KB) cells were grown in DMEM basal medium (GE Healthcare Life Science) with 1% penicillin/streptomycin, and 6% FBS. All cell cultures were maintained at 37°C in a humidified atmosphere containing 5% CO_2.

A sample of 88 EV strains, comprising 23 reference strains and 65 clinical isolates, recovered from patient specimens (CSF, stool or throat) was used in the study (**Table S1**). Virus stocks were prepared with KB (coxsackievirus B) and RD cells (other EVs) and stored at −20°C. Titration of viral suspensions was done using our end point dilution assay (Bailly *et al*., 1991). The cell cultures were inoculated at a multiplicity of infection (MOI) of 5 for 1 h at 37°C in all experiments; after washing with PBS, they were incubated for the indicated times.

Extraction of nucleic acids and EV real-time RT-qPCR. Nucleic acids were extracted from 200 µl from supernatants or the whole cells and supernatant using the NucliSens®EasyMAG™ extractor (bioMérieux) and were eluted with 25 µl of the elution buffer provided by the manufacturer. A previously described competitive internal control was added during the extraction step and amplified in our in-house RT-qPCR assay (Volle *et al*., 2012).

Viability of infected hCMEC/D3 cells. Cells were infected separately by 15 EV strains. After two washes at 24 h p.i., the cells were detached, centrifuged for 10 min at 1000g, stained with

335 the Apoptotic/Necrotic/Healthy Cells Detection Kit (Promokine), and analysed by flow
336 cytometry (BD-LSRII, BD Bioscience). Cells were considered as being viable when only
337 stained with the Hoechst compound, apoptotic when only stained with the Annexin V
338 conjugated antibody, or necrotic when they were stained with both Annexin V and ethidium
339 homodimere III. Cell fragments were detected through ethidium homodimere III staining
340 alone.

341 **Fluorescent microscopy.** HCMEC/D3 cells were grown in chamber slides, infected for 6
342 hours by different EV strains, and fixed with 4% paraformaldehyde for 10 min. For
343 mitochondria staining, the cells were incubated at 37°C for 1 h before fixation, with complete
344 EBM-2 medium containing 50 nM of MitoTracker® Mitochondrion-Selective probe M7510
345 (Invitrogen) in a humidified atmosphere of 5% CO_2. Cells were permeabilized with 0.5%
346 Triton X100 in PBS for 5 min, saturated for 10 min with 5% BSA in PBS, and incubated
347 overnight at 4°C with mouse primary monoclonal antibodies against the EV capsid protein
348 VP1 (Diagnostic Hybrid). After three PBS washes, incubation was pursued for 1 h at 37°C in
349 a solution of anti-mouse secondary antibodies conjugated to Dyelight488 (Anticorps enligne).
350 In the tests for which active mitochondria staining was not required, red-phalloïdin used for
351 actin staining was included in the secondary antibody solution. After three PBS washes, nuclear
352 DNA was counterstained with a Hoechst solution (Promokine). The slides were mounted with
353 coverslips and observed with an epifluorescence microscope (Olympus BX41) or scanning
354 confocal microscope (LSM 510, Carl Zeiss MicroImaging Inc.). Automated image analysis
355 (FIJI software) was used to calculate the number of infected cells.

356 **EV crossing through an *in vitro* model of brain microvascular endothelial barrier.** To
357 obtain microvascular endothelial barriers, hCMEC/D3 cells were cultured on a permeable
358 membrane (0.4 µm pore) placed in the upper chamber of a Transwell® device (12-well plate,
359 Corning). The upper chamber was seeded with 40,000 cells/cm² and incubated for 5 to 7 days

360 to obtain a tight confluent cell monolayer. In this *in vitro* model, the cells are polarized and
361 display a luminal side and an abluminal side (Weksler *et al*., 2005). The luminal sides of non-
362 permeable barriers were exposed separately to various EV strains, the infected barriers were
363 incubated for the indicated times, and permeability was determined at each time p.i. (see
364 below). The yield of infectious particles and the total amount of viral genome released through
365 the abluminal and luminal sides were determined as described above.
366 **Lucifer Yellow permeability assay.** The paracellular seal of the endothelial barrier was
367 determined in triplicate by testing the permeability to the Lucifer Yellow marker (LY, Sigma).
368 The cell monolayers were washed twice with collecting buffer consisting of HBSS (GE
369 Healthcare Life Science) supplemented with 1% of HEPES (GE Healthcare Life Science) and
370 1% of sodium pyruvate (GE Healthcare Life Science). The LY marker (50 µM; 400 µl) was
371 added to the upper chamber. Cells were incubated at 37°C (5% CO_2 and 100% humidity) in
372 three successive collecting wells, each containing 1.6 ml of collecting buffer, for respectively
373 10, 15, and 20 min. The LY concentration in the collecting buffer of each well and the stock
374 LY solution were determined by fluorometry. Parallel negative control tests were performed
375 with cell-free collagen-coated culture membranes. Samples were analysed in black 96-well
376 microtiter plates using a Fluoroskan Ascent FL fluorometer (Thermo Electron Corporation,
377 France) at 485 and 538 nm wavelengths for excitation and emission, respectively.
378 **Scanning and transmission electron microscopy (SEM and TEM).** The endothelial barriers
379 were washed with 0.2M Na cacodylate buffer (NCB; pH 7.4) and fixed overnight at 4°C in
380 1.6% glutaraldehyde-NCB. The cells were fixed for 1 h with 1% OsO_4 in NCB. For SEM
381 preparation, cells were dehydrated in graded ethanol, followed by critical point drying with
382 100% ethanol and hexamethyldisilasane (1:1) for 10 min, sputter-coated with gold (JEOL JFC-
383 1300), and observed at 5kV with a JEOL 6060-LV microscope. For TEM preparation, cells
384 were dehydrated in graded ethanol, infiltrated sequentially with three mixtures of

ethanol/EPON resin (2:1, 1:1, and 1:2) for 1 h each, embedded in EPON resin overnight at room temperature, and cured 2 days in a 60°C oven. Thin sections (70 nm, UC6 ultramicrotome, Leica) were stained with uranyl acetate and Pb citrate, and observed at 80 kV with a Hitachi H-7650 microscope. All chemical products were provided by Delta Microscopies.

Statistical Analysis. Statistical analyses were made with software Stata (version 12, StataCorp, College Station, US). Tests were two-sided, with a type I error set at a=0.05. Quantitative data are expressed as means (and associated standard deviation, Gaussian distribution verified by the Shapiro-Wilk test). Correlated data were analysed by mixed models to study the evolution of parameters taking into account between and within strain variability (random effects such as intercept and slope). These analyses were completed by ANOVA for repeated measures followed by post-hoc Tukey-Kramer test. Principal component analysis was done to explore the relation between several quantitative parameters. Correlation coefficients (Pearson or Spearman when appropriate) were calculated to quantify these relations.

400 **LEGENDS TO FIGURES**

401 **Fig. 1. Heterogeneity of enterovirus infection in hCMEC/D3 cells.** Replication in
402 hCMEC/D3 cells of EV strains selected among species, types, and genogroups was examined
403 at 24 h p.i. (a) Data are represented as means of two independent assays and given as the
404 number of viral genome copies per cell (x-axis) and of infectious particles per cell (y-axis).
405 Correlation between the yield of virus genome and yield of infectious virus is indicated. (b)
406 Replication kinetics of virus strains of four EV types in hCMEC/D3 cells. Data are
407 representative of means of three independent replicates for each virus E-30 (●), E-6 (▲), E-12
408 (♦), and EV-A71 (×). (c) Susceptibility spectrum of the hCMEC/D3 cell line to EVs estimated
409 as the proportion of infected cells at 6 h p.i. A sample of 24 viral strains representing 19
410 different types was tested. Green and blue fluorescence indicate the VP1 protein and the nuclei,
411 respectively. Scale bar, 100 µm. Data are represented as mean ± SD of three experiments. (d)
412 Comparison of cell mortality rates at 24 h p.i. (n=15 EV strains). Data are represented as mean
413 ± SD of four independent experiments. The blue line indicates the cell mortality rate (10%) in
414 mock-infected cells (NoV).

415

416 **Fig. 2. Principal component analysis of enterovirus replication in hCMEC/D3 cells.**
417 Ordination of the data obtained for 15 EV strains using principal component analysis. The
418 horizontal axis is linked to cell sensitivity to EVs and the vertical axis to virus production.

419

420 **Fig. 3. Disruption of a microvascular endothelial barrier during enterovirus infection.**
421 Endothelial barriers of hCMEC/D3 cells produced on Transwell® membranes were infected
422 with E-6/CF2660-01 (a), E-11/CF228046-07 (b), E-12/CF1157-91 (c), E-30/CF2575-00 (d),
423 EV-71/CF166105-10 (e), and EV-A71/CF160019-10 (f). At the indicated time points, the
424 culture mediums in the luminal and abluminal compartments were collected and stored

separately. Paracellular permeability was measured. Data are indicated as mean ± SD of three experiments. The number of EV genome copies and infectious virus particles are respectively indicated with white and light grey bars for the luminal compartment, and respectively with dark grey and dashed bars for the abluminal compartment. Permeability coefficients for mock infected and infected barriers are indicated with green and red lines, respectively.

Fig. 4. Disruption of endothelial barriers during enterovirus infection. The hCMEC/D3 barriers were analysed with SEM at 24 h p.i. Representative fields of duplicate experiments are shown: mock-infected monolayers (a–c), and barriers infected with E-6/CF2660-01 (d–f), E-12/CF1157-91 (g–i), E-30/CF2575-00 (j–l), and EV-A71/CF166105-10 (m–o). White arrow head, breach of the endothelial barriers; red and green arrow heads, cells with a necrotic and an apoptotic shape, respectively; blue arrow head, round cell with no sign of altered plasma membrane.

Fig. 5. Ultrastructural features at 24 h p.i. of hCMEC/D3 barriers infected with an E-6 strain. The infected hCMEC/D3 barriers were observed at low magnification with TEM (a and b). Virus-induced reorganization of cytoplasmic elements (c). Features of the vesicular structures (d). Dense electron punctuation suggestive of virus aggregates (e). Bars, 4 µm (a and b); 500 nm (c–e). Representative fields of duplicate experiments are shown; mock-infected cells are shown in figure S4. Abbreviations: N, nucleus; M, mitochondria; MC, membranous replication complex; A, autolysosome/amphisome; V, virus aggregates.

Fig. 6. Ultrastructural features at 24 h p.i. of hCMEC/D3 barriers infected with an EV-A71 strain. The infected hCMEC/D3 barriers were analysed at low magnification with TEM; unaltered cells (a and b) and altered cells with virus-induced vesicular structures (c and d).

Features of the vesicular structures (e–i). Bar, 10 µm (a–d); 1 µm (e and f); 500 nm (g–i). Representative fields of duplicate experiments are shown; mock-infected cells are shown in figure S4. Abbreviations: N, nucleus; M, mitochondria; MC, membranous replication complex.

Fig. 7. The actin cytoskeleton network is disrupted in enterovirus-infected hCMEC/D3 cells. The hCMEC/D3 cells were analysed at 6 h p.i. during replication of strains E-12/CF1157-91 (a–c), E-6/CF2660-01 (d–i), E-30/CF2575-00 (j–l), E-11/CF228046-07 (m–o), and EV-A71/CF166105-10 (p–r); mock-infected cells (s–u). Actin network is shown in red, VP1 capsid protein in green, and nuclei in blue. Bars represent 10 µm. White arrow heads indicate intermediate disruption of actin cytoskeleton.

Fig. 8. Perinuclear relocation of active mitochondria in enterovirus-infected hCMEC/D3 cells. The hCMEC/D3 cells were analysed at 6 h p.i. during replication of E-12/CF1157-91 (a–c), E-6/CF2660-01 (d–f), E-30/CF2575-00 (g–i), E-11/CF228046-07 (j–l), and EV-A71/CF166105-10 (m–o); mock-infected cells (s–u). Active mitochondria are shown in red, VP1 capsid protein in green, and nuclei in blue. Bars represent 10 µm. White and yellow arrow heads indicate dense clusters and intermediate clustering of mitochondria, respectively.

ACKNOWLEDGEMENTS

The authors acknowledge the technical contribution of Gwendoline Jugie, Nathalie Rodde, and Isabelle Simon for helpful assistance in virus culture and sequencing. We thank Mr. Jeffrey Watts for help with preparing the English manuscript. Fluorescence confocal microscopy observations were done at the ICCF (Imagerie Confocale de Clermont-Ferrand) Centre, France. TEM and SEM observations were done at the Centre d'Imagerie Cellulaire Santé (Clermont-Ferrand, France).

REFERENCES

Agol, V. I. & Gmyl, A. P. (2010). Viral security proteins: counteracting host defences. *Nat Rev Microbiol* **8**, 867–878.

Antona, D., Lévêque, N., Chomel, J. J., Dubrou, S., Lévy-Bruhl, D. & Lina, B. (2007). Surveillance of enteroviruses in France, 2000-2004. *Eur J Clin Microbiol Infect Dis* **26**, 403–412.

Bailly, J. L., Chambon, M., Peigue-Lafeuille, H., Laveran, H., De Champs, C. & Beytout, D. (1991). Activity of glutaraldehyde at low concentrations (less than 2%) against poliovirus and its relevance to gastrointestinal endoscope disinfection procedures. *Appl Environ Microbiol* **57**, 1156–1160.

Belov, G. A., Nair, V., Hansen, B. T., Hoyt, F. H., Fischer, E. R. & Ehrenfeld, E. (2012). Complex dynamic development of poliovirus membranous replication complexes. *J Virol* **86**, 302–312.

Bergelson, J. M., Chan, M., Solomon, K. R., St John, N. F., Lin, H. & Finberg, R. W. (1995). Decay-accelerating factor (CD55), a glycosylphosphatidylinositol-anchored complement regulatory protein, is a receptor for several echoviruses. *PNAS (USA)* **91**, 6245–6248.

Bergelson, J. M., St John, N., Kawaguchi, S., Chan, M., Stubdal, H., Modlin, J. & Finberg, R. W. (1993). Infection by Echoviruses 1 and 8 Depends on the cx2 Subunit of Human VLA-2. *J Virol* **67**, 6847–6852.

Bozym, R. A., Morosky, S. A., Kim, K. S., Cherry, S. & Coyne, C. B. (2010). Release of intracellular calcium stores facilitates coxsackievirus entry into polarized endothelial cells. *PLoS Pathog* **6**, e1001135.

Conaldi, P. G., Serra, C., Mossa, A., Falcone, V., Basolo, F., Camussi, G., Dolei, A. & Toniolo, A. (1997). Persistent infection of human vascular endothelial cells by group B coxsackieviruses. *J Infect Dis* **175**, 693-696.

Chen, C. S., Yao, Y. C., Lin, S. C., Lee, Y. P., Wang, Y. F., Wang, J. R., Liu, C. C., Lei, H. Y. & Yu, C. K. (2007). Retrograde axonal transport: a major transmission route of enterovirus 71 in mice. *J Virol* **81**, 8996–9003.

Cheng, H. Y., Huang, Y. C., Yen, T. Y., Hsia, S. H., Hsieh, Y. C., Li, C. C., Chang, L. Y., & Huang, L. M. (2014). The correlation between the presence of viremia and clinical severity in patients with enterovirus 71 infection: a multi-center cohort study. *BMC Infect Dis* **14**, 417.

Coyne, C. B., Kim, K. S. & Bergelson, J. M. (2007). Poliovirus entry into human brain microvascular cells requires receptor-induced activation of SHP-2. *EMBO J* **26**, 4016–4028.

Eberle, K. E., Nguyen, V. T. & Freistadt, M. S. (1995). Low levels of poliovirus replication in primary human monocytes: possible interactions with lymphocytes. *Arch Virol* **140**, 2135-2150.

Engelhardt, B. & Coisne, C. (2011). Fluids and barriers of the CNS establish immune privilege by confining immune surveillance to a two-walled castle moat surrounding the CNS castle. Fluids and Barriers of the CNS **8**, 4.

Gromeier, M., & Wimmer E. (1998). Mechanism of injury-provoked poliomyelitis. J Virol **72**, 5056–5060.

Haddad, A., Nokhbeh, M. R., Alexander, D. A., Dawe, S. J., Grisé, C., Gulzar, N. & Dimock, K. (2004). Binding to decay-accelerating factor is not required for infection of human leukocyte cell lines by enterovirus 70. *J Virol* **78**, 2674-2681.

Khetsuriani, N., Lamonte-Fowlkes, A., Oberste, S. & Pallansch, M. A. (2006). Centers for Disease Control and Prevention. Enterovirus surveillance-United States, 1970-2005. *MMWR Surveill Summ* **55**, 1–20.

Kim, S., Kim, H. Y., Lee, S., Kim, S. W., Sohn, S., Kim, K. & Cho, H. (2007). Hepatitis B virus x protein induces perinuclear mitochondrial clustering in microtubule- and Dynein-dependent manners. *J Virol* **81**, 1714–1726.

Khong, W. X., Yan, B., Yeo, H., Tan, E. L., Ng, J. K. W., Chow, V. T. & Alonso, S. (2012). A non-mouse-adapted enterovirus 71 (EV71) strain exhibits neurotropism, causing neurological manifestations in a novel mouse model of EV71 infection. *J Virol* **86**, 2121–2131.

Lancaster, K. Z., & Pfeiffer, J. K. (2010). Limited trafficking of a neurotropic virus through inefficient retrograde axonal transport and the type I interferon response. *PLoS Pathog* **6**, e1000791.

Liang, C. C., Sun, M. J., Lei, H. Y., Chen, S. H., Yu, C. K., Liu, C. C., Wang, J. R., & Yeh TM. (2004). Human endothelial cell activation and apoptosis induced by enterovirus 71 infection. *J Med Virol* **74**, 597-603.

Limpens, R. W., van der Schaar, H. M., Kumar, D., Koster, A. J., Snijder, E. J., van Kuppeveld, F. J. & Bárcena, M. (2011). The transformation of enterovirus replication structures: a three-dimensional study of single- and double-membrane compartments. *MBio* **2**, 00166–11.

Merilahti, P., Koskinen, S., Heikkilä, O., Karelehto, E. & Susi, P. (2012). Endocytosis of integrin-binding human picornaviruses. *Adv Virol* **2012**, 547530.

Nishikawa, M., Matsubara, T., Yoshitomi, T., Ichiyama, T., Hayashi, T. & Furukawa, S. (2000). Abnormalities of brain perfusion in echovirus type 30 meningitis. J Neurol Sci **179**, 122 – 126.

Ohka, S., Nihei, C., Yamazaki, M. & Nomoto, A. (2012). Poliovirus trafficking toward central nervous system via human poliovirus receptor-dependent and –independent pathway. *Frontiers Microbiol* **2012**, 00147.

Rotbart, H. A. (1995). Meningitis and encephalitis. In Human enterovirus infections, pp 271-289. Edited by H. A. Rotbart. Washington D. C., ASM Press.

Ren, R. & Racaniello, V. R. (1992). Poliovirus spreads from muscle to the central nervous system by neural pathways. *J Infect Dis* **166**, 747–752.

Rojo, G., Chamorro, M., Salas, M. L., Viñuela, E., Cuezva, J. M. & Salas, J. (1998). Migration of mitochondria to viral assembly sites in African swine fever virus-infected cells. *J Virol* **72**, 7583–7588.

Sabin, A. B. (1956). Pathogenesis of poliomyelitis; reappraisal in the light of new data. *Science* **123**, 1151-1157.

Saijets, S., Ylipaasto, P., Vaarala, O., Hovi, T., & Roivainen, M. (2003). Enterovirus infection and activation of human umbilical vein endothelial cells. *J Med Virol* **70**, 430-439.

Spindler, K. R. & Hsu, T. H. (2012). Viral disruption of the blood-brain barrier. *Trends Microbiol* **20**, 282–290.

Stamatovic, S. M., Sladojevic, N., Keep, R. F. & Andjelkovic, A. V. (2012). Relocalization of junctional adhesion molecule A during inflammatory stimulation of brain endothelial cells. *Mol Cell Biol* **32**, 3414–3427.

Tabor-Godwin, J. M., Ruller, C. M., Bagalso, N., An, N., Pagarigan, R, R., Harkins, S., Gilbert, P. E., Kiosses, W. B., Gude, N. A., Cornell, C. T. & other authors (2010). A novel population of myeloid cells responding to coxsackievirus infection assists in the dissemination of virus within the neonatal CNS. J Neurosci **30**, 8676–8691.

Verma, S., Kumar, M., Gurjav, U., Lum, S., Nerurkar, V. R. (2010). Reversal of West Nile virus-induced blood-brain barrier disruption and tight junction proteins degradation by matrix metalloproteinases inhibitor. *Virology* **397**,130-138.

Verma, S., Lo, Y., Chapagain, M., Lum, S., Kumar, M., Gurjav, U., Luo, H., Nakatsuka, A. & Nerurkar, V. R. (2009). West Nile virus infection modulates human brain microvascular endothelial cells tight junction proteins and cell adhesion molecules: Transmigration across the in vitro blood-brain barrier. *Virology* **385**, 425-433.

Volle, R., Bailly, J. L., Mirand, A., Pereira, B., Marque-Juillet, S., Chambon, M., Regagnon, C., Brebion, A., Henquell, C. & other authors (2014). Variations in cerebrospinal fluid viral loads among enterovirus genotypes in patients hospitalized with laboratory-confirmed meningitis due to enterovirus. *J Infect Dis* **210**, 576–584.

Volle, R., Nourrisson C., Mirand, A., Regagnon, C., Chambon, M., Henquell, C., Bailly, J. L., Peigue-Lafeuille, H. & Archimbaud, C. (2012). Quantitative real-time RT-PCR assay for research studies on enterovirus infections in the central nervous system. *J Virol Methods* **185**, 142–148.

Vuorinen, T., Vainionpää, R., Vanharanta, R. & Hyypiä, T. (1996). Susceptibility of human bone marrow cells and hematopoietic cell lines to coxsackievirus B3 infection. *J Virol* **70**, 9018-9023.

Wahid, R., Cannon, M. J. & Chow, M. (2005a). Virus-specific CD4+ and CD8+ cytotoxic T-cell responses and long-term T-cell memory in individuals vaccinated against polio. *J Virol* **79**, 5988-5995.

Wahid, R., Cannon, M. J. & Chow, M. (2005b). Dendritic cells and macrophages are productively infected by poliovirus. *J Virol* **79**, 401-9.

Weksler, B., Romero, I. A. & Couraud, P. O. (2013). The hCMEC/D3 cell line as a model of the human blood brain barrier. *Fluids Barriers CNS* **10**, 16.

Weksler, B., Subileau, E. A., Perrière, N., Charneau, P., Holloway, K., Leveque, M., Tricoire-Leignel, H., Nicotra, A., Bourdoulous, S. & other authors (2005). Blood-brain barrier-specific properties of a human adult brain endothelial cell line. *FASEB J* **19**, 1872–1874.

Yang, W. X., Terasaki, T., Shiroki, K., Ohka, S., Aoki, J., Tanabe, S., Nomura, T., Terada, E., Sugiyama, Y. & Nomoto, A. (1997). Efficient delivery of circulating poliovirus to the central nervous system independently of poliovirus receptor. *Virology* **229**, 421–428.

Yen, M. H., Tsao, K. C., Huang, Y. C., Huang, C. G., Huang, Y. L., Lin, R., Chang, M. L., Huang, C. C., Yan, D. C., & Lin, T. Y. (2007). Viral load in blood is correlated with disease severity of neonatal coxsackievirus B3 infection: early diagnosis and predicting disease severity is possible in severe neonatal enterovirus infection. *Clin Infect Dis* **44**, e78–81.

Ylipaasto, P., Eskelinen, M., Salmela, K., Hovi, T. & Roivainen, M. (2010). Vitronectin receptors, αv integrins, are recognized by several non-RGD-containing echoviruses in a continuous laboratory cell line and also in primary human Langerhans' islets and endothelial cells. *J Gen Virol* **91**, 155–165.

Zanone, M. M., Favaro, E., Conaldi, P. G., Greening, J., Bottelli, A., Perin, P. C., Klein, N. J., Peakman, M. & Camussi, G. (2003). Persistent infection of human microvascular endothelial cells by coxsackie B viruses induces increased expression of adhesion molecules. *J Immunol* **171**, 438–446.

Zhang, Y., Cui, W., Liu, L., Wang, J., Zhao, H., Liao, Y., Na, R., Dong, C., Wang, L. & other authors (2011). Pathogenesis study of enterovirus 71 infection in rhesus monkeys. *Lab Invest* **91**, 1337–1350.

Figure 1

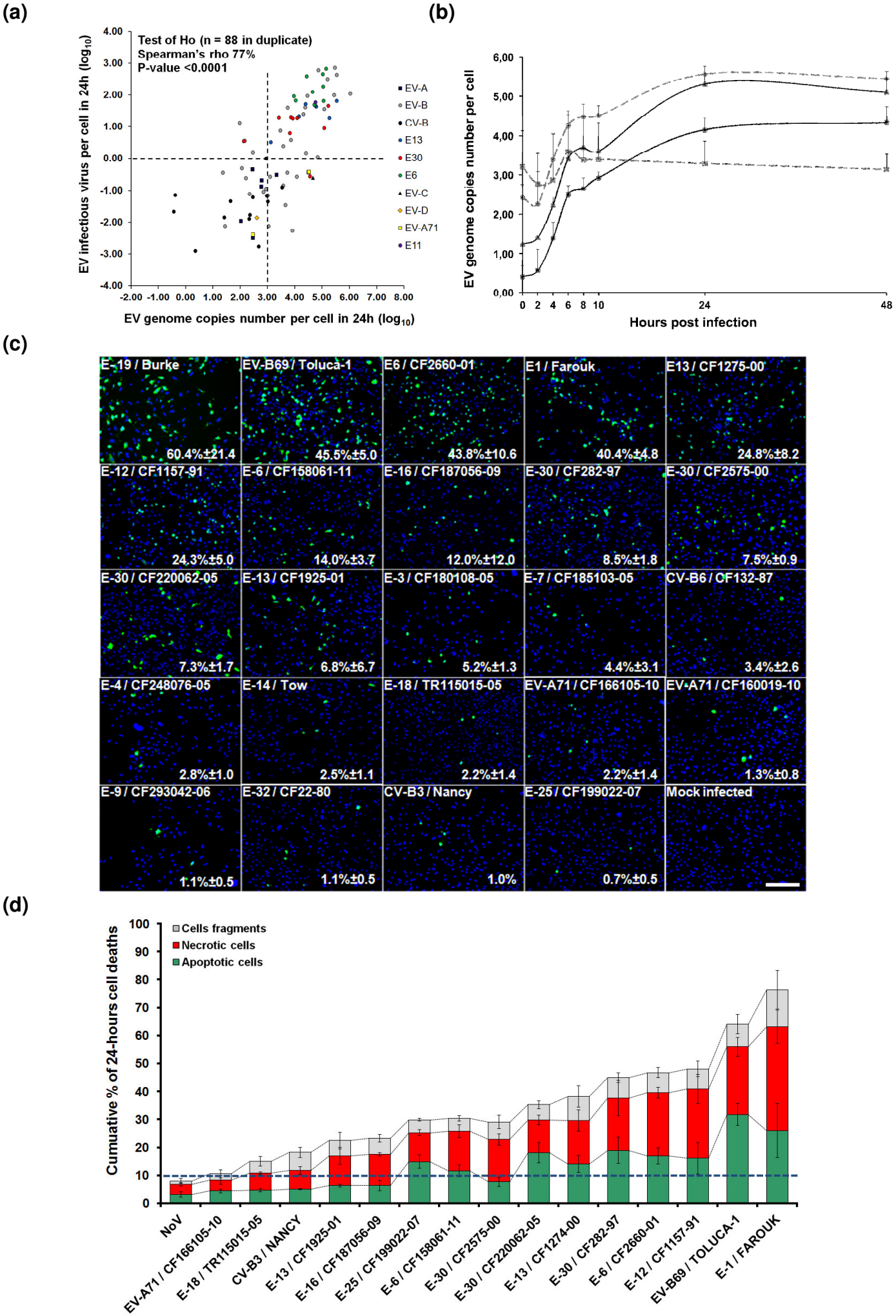
(a)
Test of Ho (n = 88 in duplicate)
Spearman's rho 77%
P-value <0.0001
EV infectious virus per cell in 24h (log10)
EV genome copies number per cell in 24h (log10)
EV-A
EV-B
CV-B
E13
E30
E6
EV-C
EV-D
EV-A71
E11
(b)
EV genome copies number per cell
Hours post infection
(c)
E-19 / Burke 60.4%±21.4
EV-B69 / Toluca-1 45.5%±5.0
E6 / CF2660-01 43.8%±10.6
E1 / Farouk 40.4%±4.8
E13 / CF1275-00 24.8%±8.2
E-12 / CF1157-91 24.3%±5.0
E-6 / CF158061-11 14.0%±3.7
E-16 / CF187056-09 12.0%±12.0
E-30 / CF282-97 8.5%±1.8
E-30 / CF2575-00 7.5%±0.9
E-30 / CF220062-05 7.3%±1.7
E-13 / CF1925-01 6.8%±6.7
E-3 / CF180108-05 5.2%±1.3
E-7 / CF185103-05 4.4%±3.1
CV-B6 / CF132-87 3.4%±2.6
E-4 / CF248076-05 2.8%±1.0
E-14 / Tow 2.5%±1.1
E-18 / TR115015-05 2.2%±1.4
EV-A71 / CF166105-10 2.2%±1.4
EV-A71 / CF160019-10 1.3%±0.8
E-9 / CF293042-06 1.1%±0.5
E-32 / CF22-80 1.1%±0.5
CV-B3 / Nancy 1.0%
E-25 / CF199022-07 0.7%±0.5
Mock infected
(d)
Cumulative % of 24-hours cell deaths
Cells fragments
Necrotic cells
Apoptotic cells
NoV
EV-A71 / CF166105-10
E-18 / TR115015-05
CV-B3 / NANCY
E-13 / CF1925-01
E-16 / CF187056-09
E-25 / CF199022-07
E-6 / CF158061-11
E-30 / CF2575-00
E-30 / CF220062-05
E-13 / CF1274-00
E-30 / CF282-97
E-6 / CF2660-01
E-12 / CF1157-91
EV-B69 / TOLUCA-1
E-1 / FAROUK

Figure 2

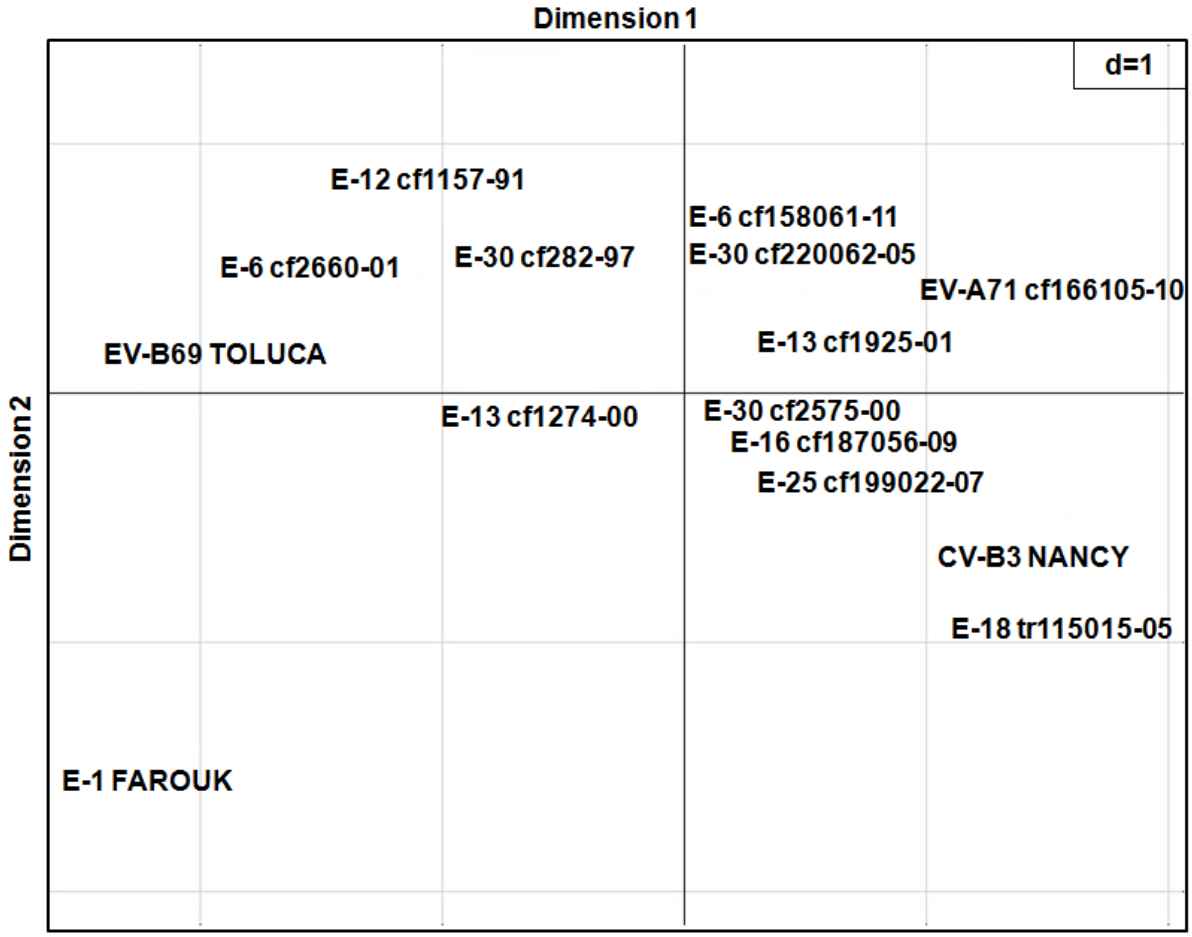
Dimension 1
Dimension 2
d=1
E-12 cf1157-91
E-6 cf158061-11
E-30 cf220062-05
E-6 cf2660-01
E-30 cf282-97
EV-A71 cf166105-10
EV-B69 TOLUCA
E-13 cf1925-01
E-13 cf1274-00
E-30 cf2575-00
E-16 cf187056-09
E-25 cf199022-07
CV-B3 NANCY
E-18 tr115015-05
E-1 FAROUK

Figure 3

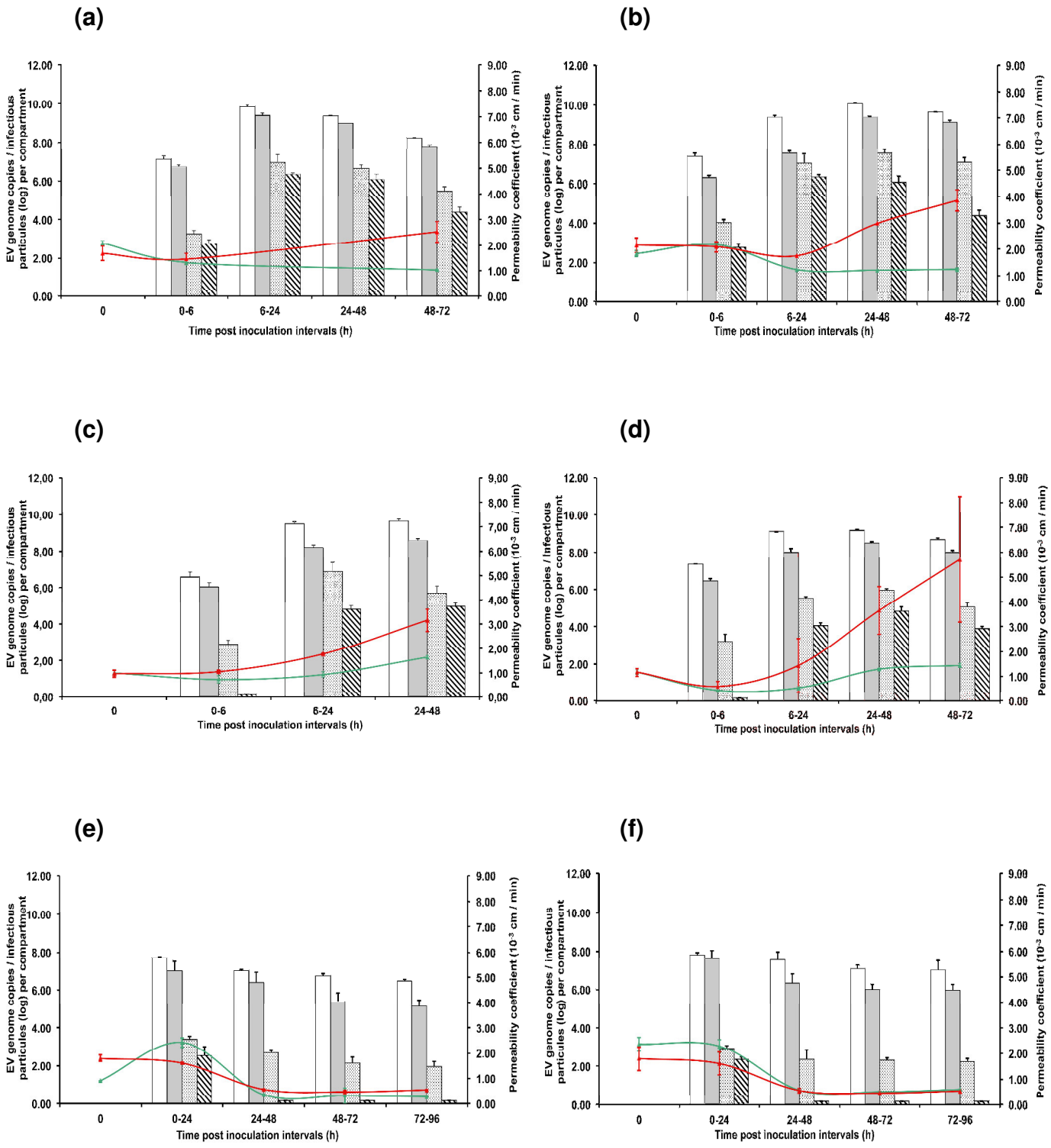
(a)
(b)
(c)
(d)
(e)
(f)
EV genome copies / infectious particules (log) per compartment
Permeability coefficient (10⁻³ cm / min)
Time post inoculation intervals (h)
0
0-6
6-24
24-48
48-72
0-24
72-96

Figure 4

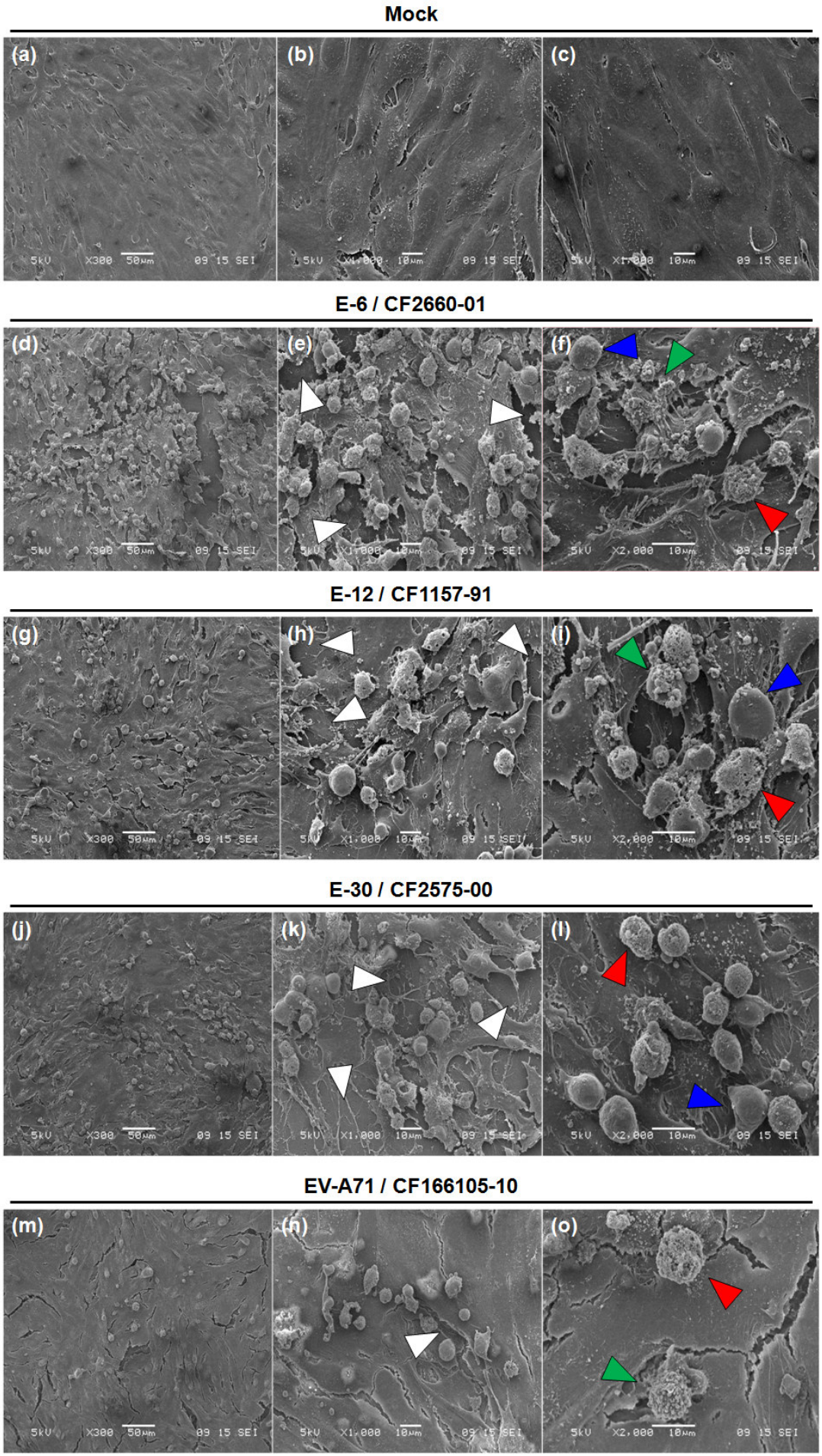
Mock
(a)
(b)
(c)
E-6 / CF2660-01
(d)
(e)
(f)
E-12 / CF1157-91
(g)
(h)
(i)
E-30 / CF2575-00
(j)
(k)
(l)
EV-A71 / CF166105-10
(m)
(n)
(o)

Figure 5

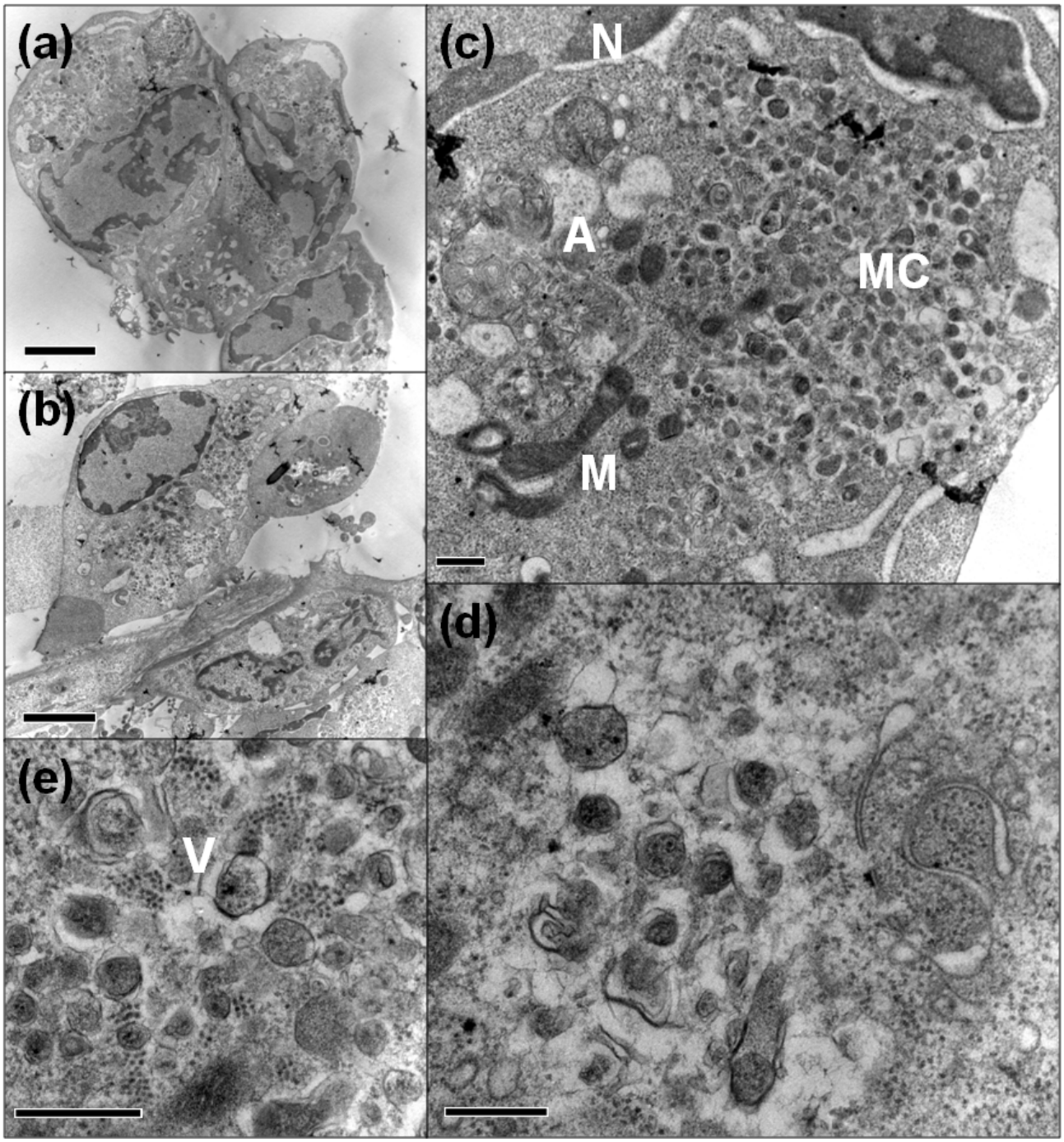

Figure 6

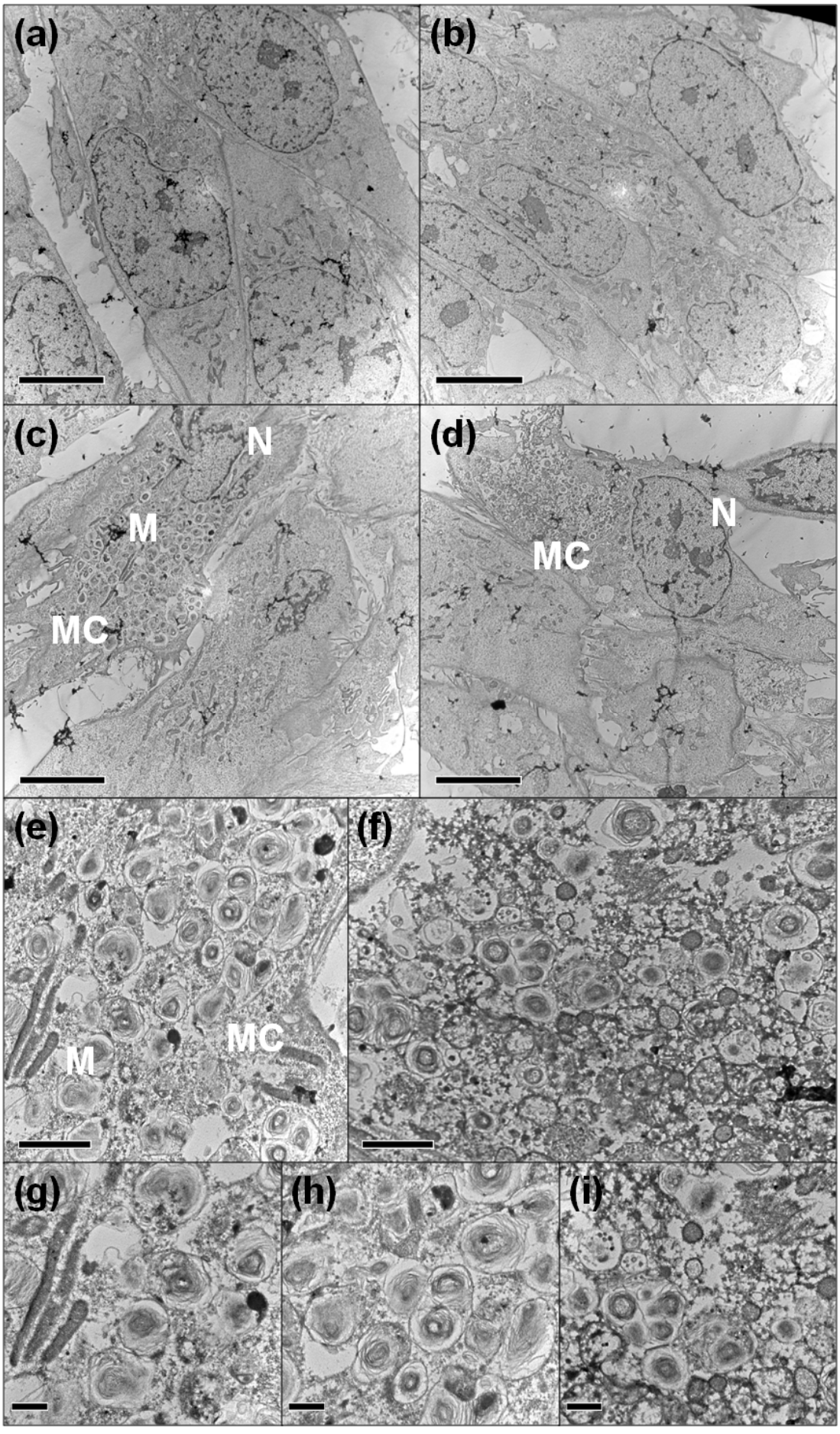

Figure 7

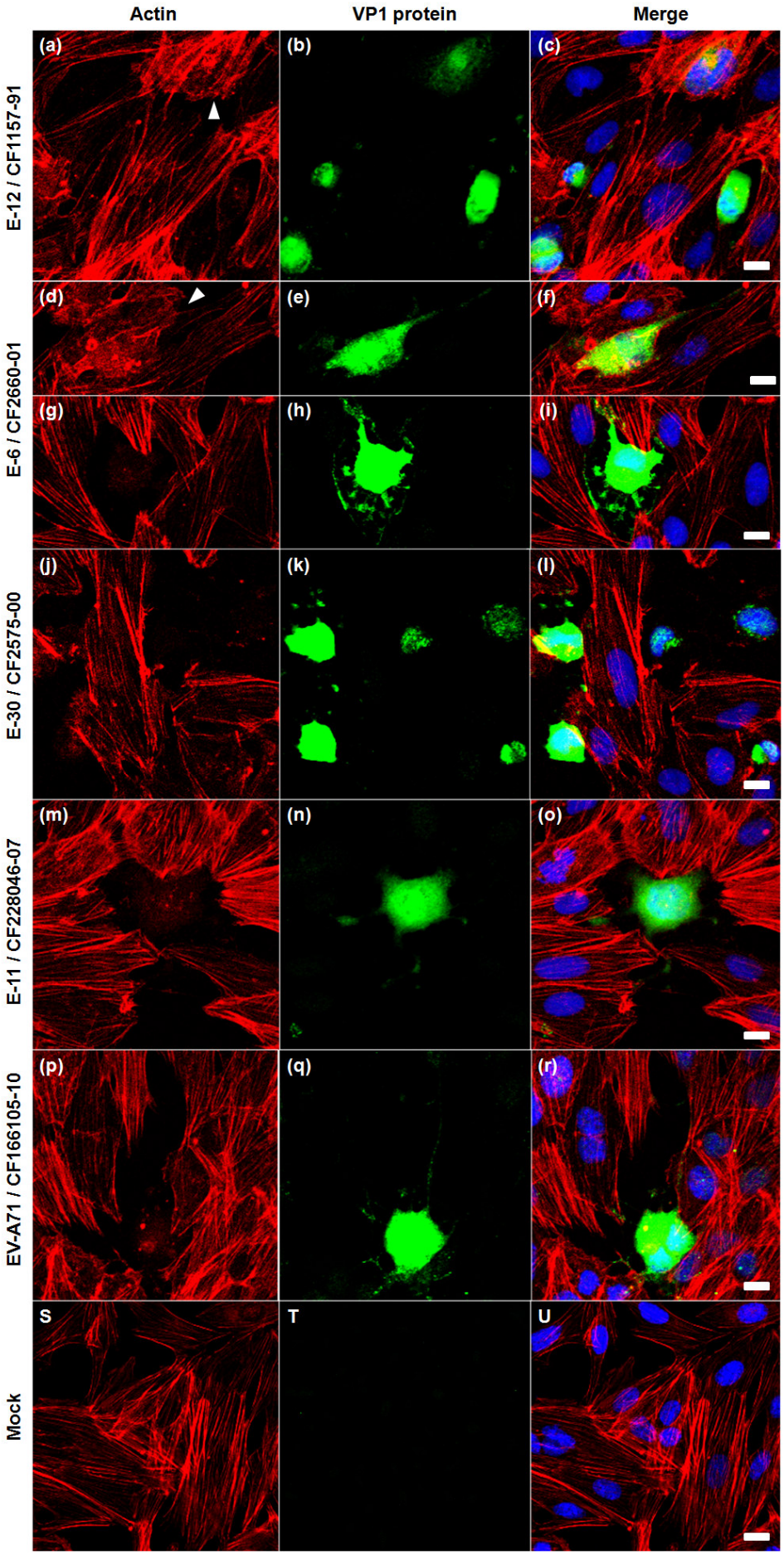
Actin
VP1 protein
Merge
E-12 / CF1157-91
E-6 / CF2660-01
E-30 / CF2575-00
E-11 / CF228046-07
EV-A71 / CF166105-10
Mock
(a)
(b)
(c)
(d)
(e)
(f)
(g)
(h)
(i)
(j)
(k)
(l)
(m)
(n)
(o)
(p)
(q)
(r)
S
T
U

Figure 8

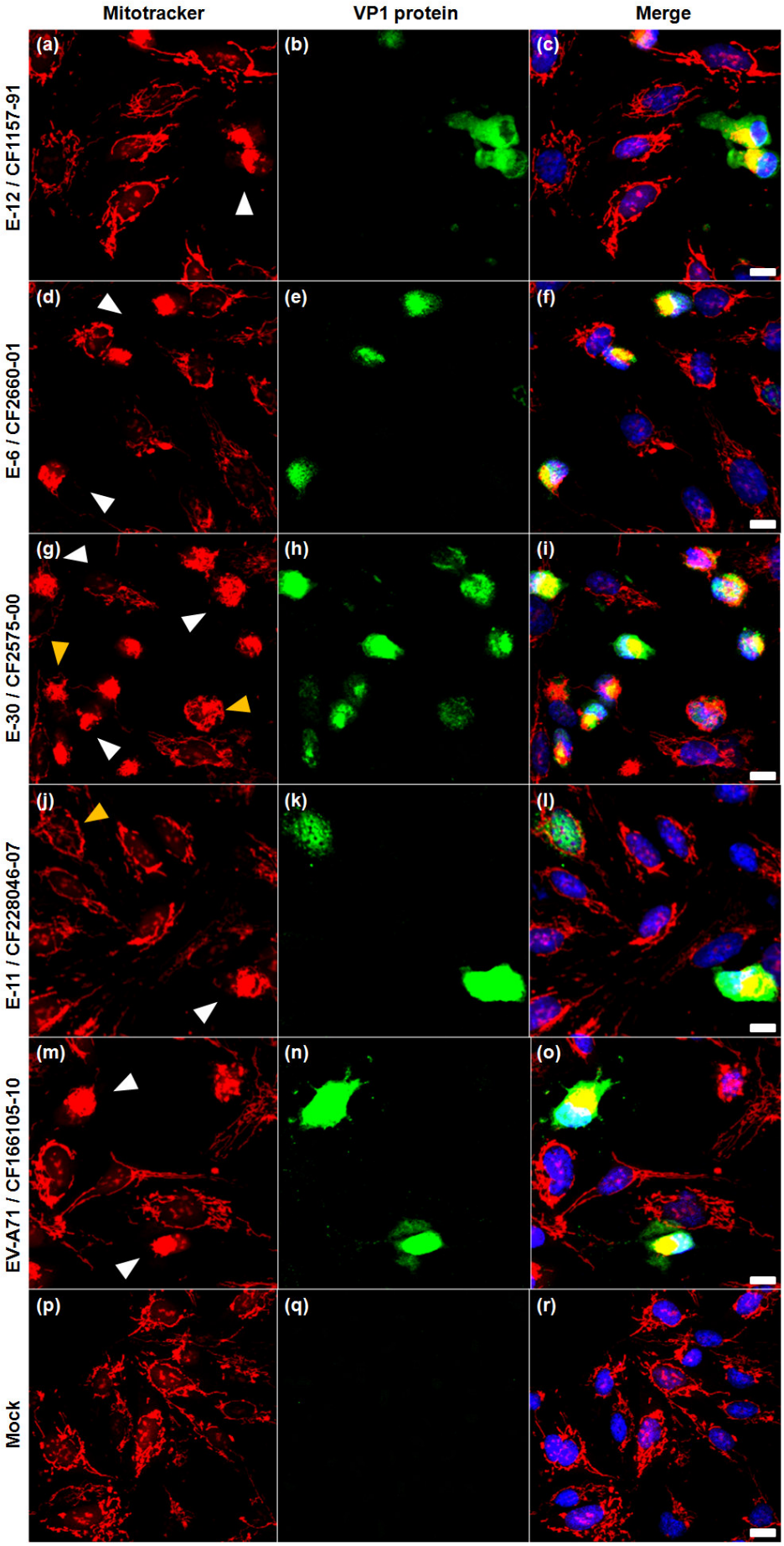
Mitotracker
VP1 protein
Merge
E-12 / CF1157-91
E-6 / CF2660-01
E-30 / CF2575-00
E-11 / CF228046-07
EV-A71 / CF166105-10
Mock
(a)
(b)
(c)
(d)
(e)
(f)
(g)
(h)
(i)
(j)
(k)
(l)
(m)
(n)
(o)
(p)
(q)
(r)

Figure S1

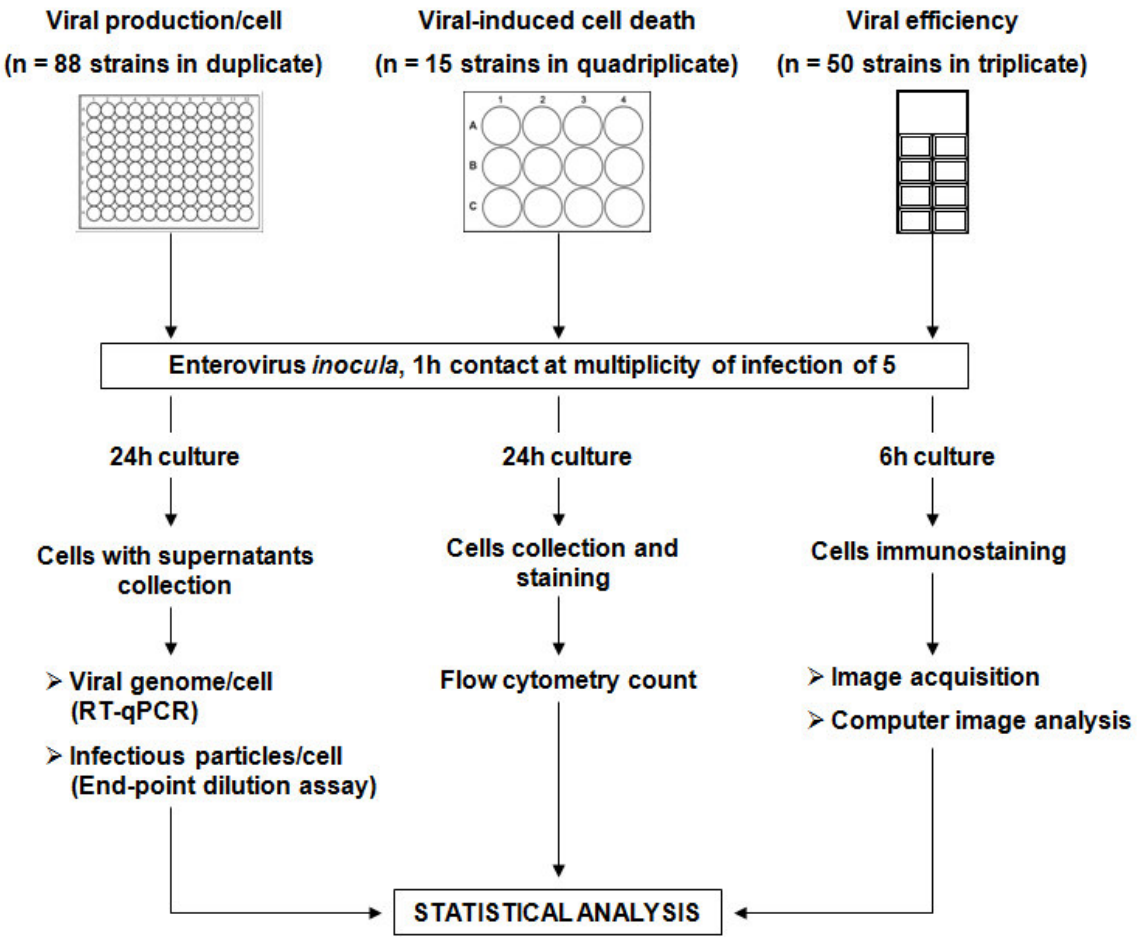

Fig. S1. Schematic representation of the strategy used for testing the susceptibility of hCMEC/D3 cells to a large array of enterovirus types. Virus production per cell was assessed in hCMEC/D3 cells cultured in 96-wells plates. A total of 88 different EV strains were tested in two independent replicates. The whole cell monolayers and supernatants were harvested at 24 h p.i. The amount of viral genomes and infectious particles were quantified by RT-qPCR and viral titration respectively. Cell mortality was analysed during virus infection of hCMEC/D3 cells cultured in 12-well plates; 15 EV strains were compared in 4 independent replicates. Cells were collected, stained for apoptosis and necrosis testing, and counted by flow cytometry at 24 h p.i. Infection efficiency was assessed in cells cultured in 8-well labtek® culture slides. The hCMEC/D3 cells were inoculated with 50 different EV strains. At 6 h p.i., before massive release of progeny viruses, cells were fixed, immunostained for viral protein VP1 and nuclear DNA, and observed at low magnification (10X) with an epifluorescence microscope. The pictures were then analysed to determine the proportion of infected cells.

Figure S2

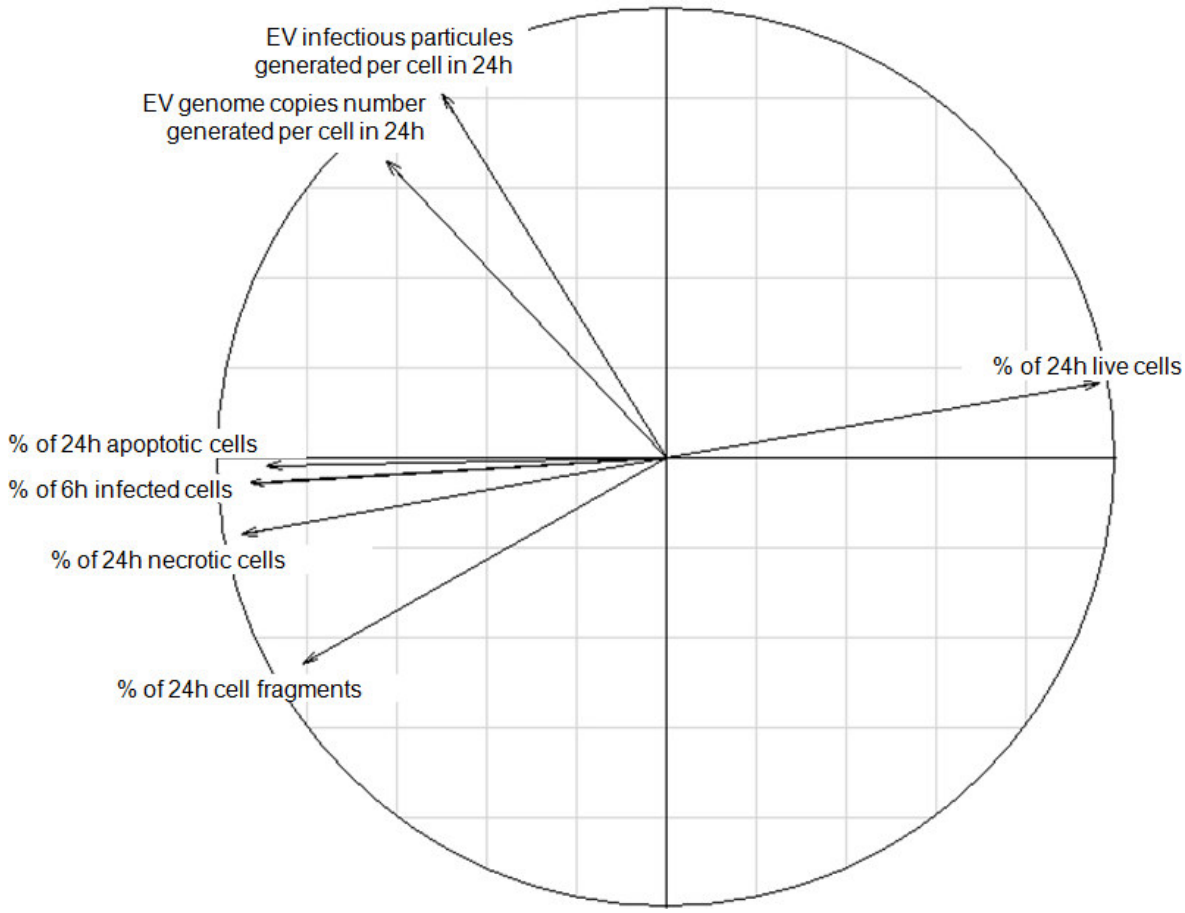

Fig. S2. Correlation circle of the principal component analysis showing the variables linked with horizontal and vertical axis.

Figure S3

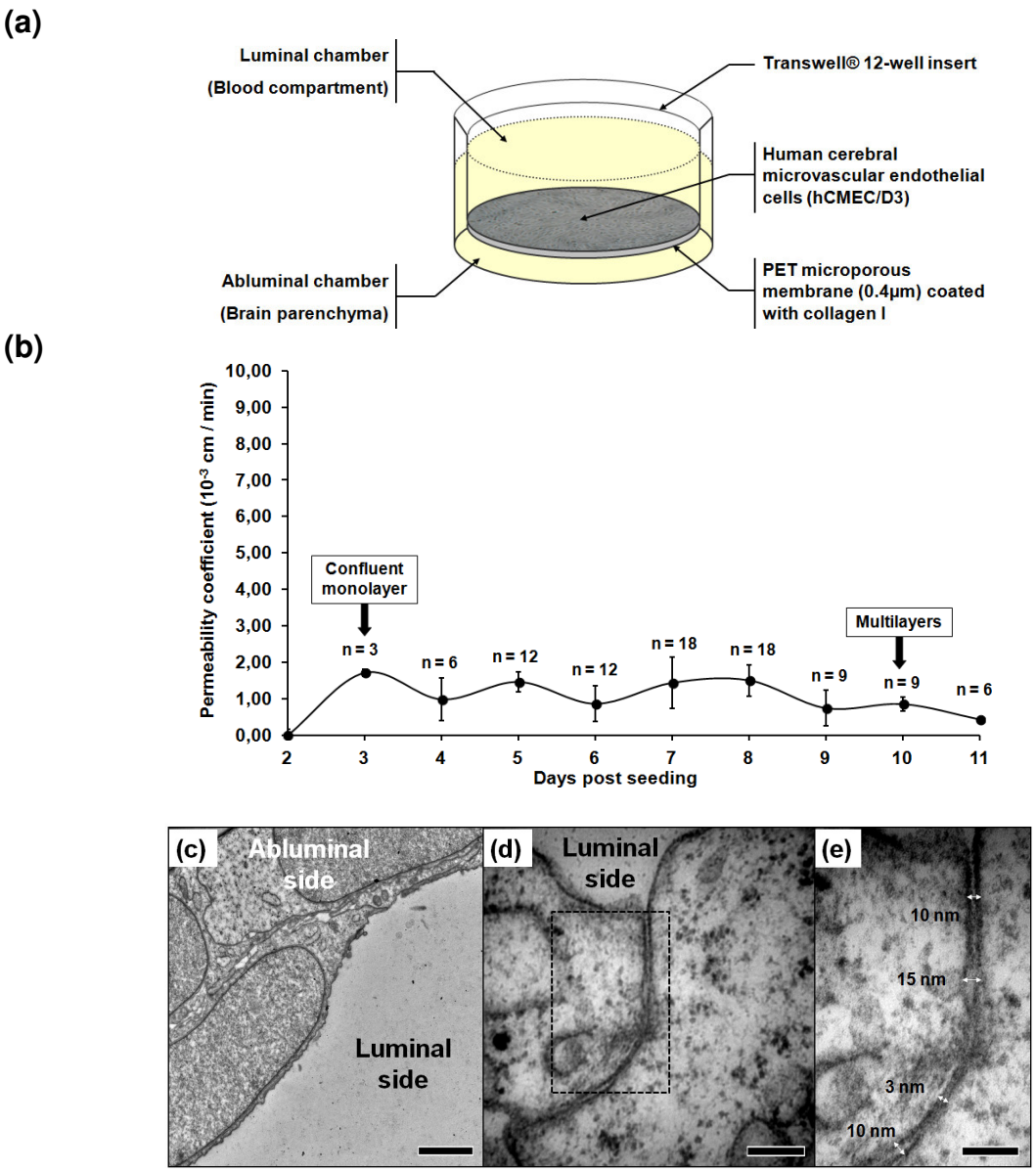

Fig. S3. In vitro model of brain endothelial barrier of polarized hCMEC/D3.

Schematic representation of the model of a blood-brain endothelial barrier obtained by culture of hCMEC/D3 cells at the surface of a permeable membrane (0.4 µm pore; coated with rat collagen-I) included within the upper chamber of a Transwell® device (a). Lucifer yellow (LY) paracellular permeability was measured for 11 days after seeding cells in different independent experiments representative of triplicate cultures (b). Transverse observations by transmission electron microscopy of a polarized hCMEC/D3 cell monolayer (culture of 7 days), scale bar 2 µm (c). Intercellular junction, scale bar 200 nm (d), with a high magnification showing an electron-dense tight junction, with the measurements of intercellular spaces, scale bar 100 nm (e).

Figure S4

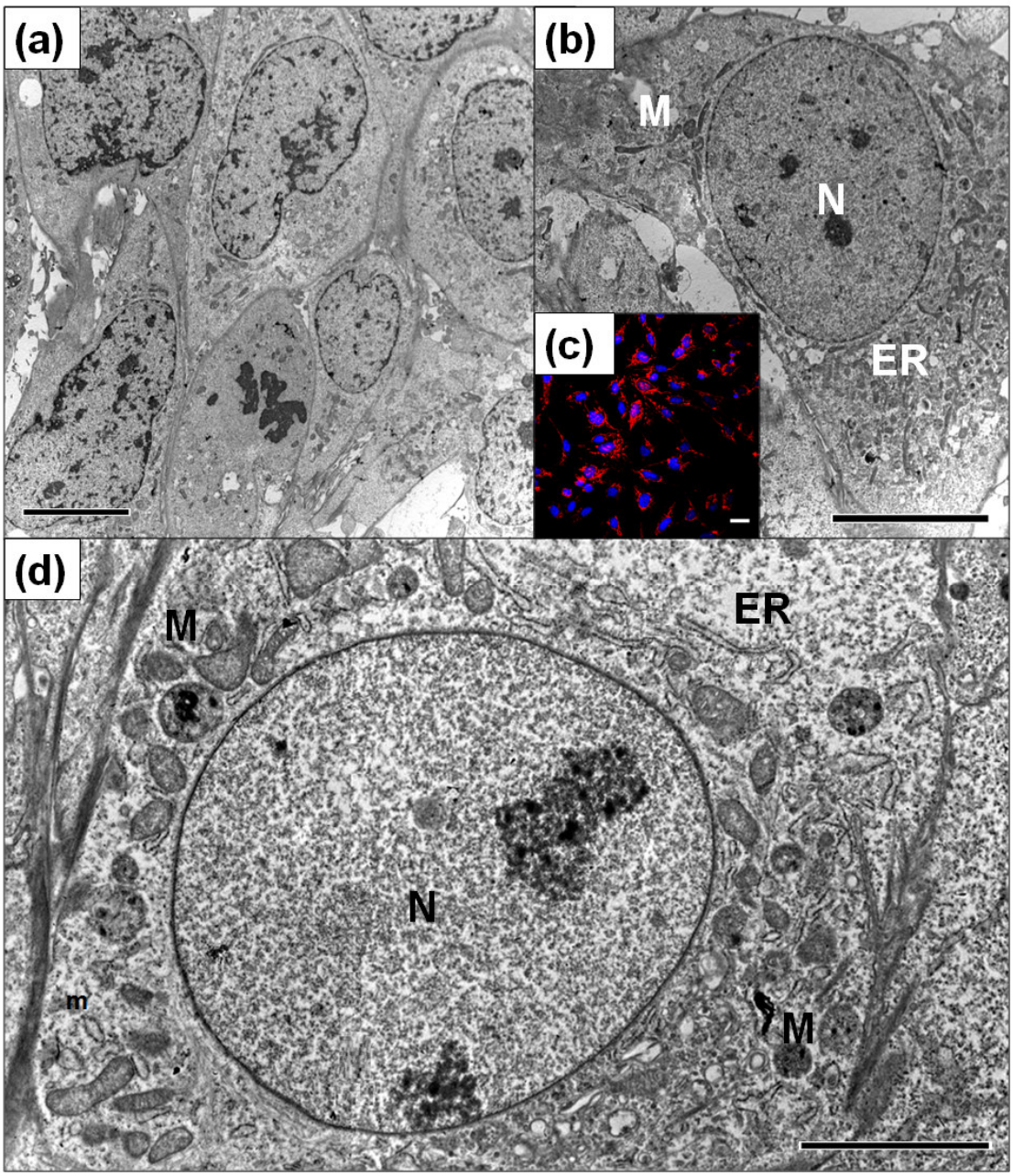

Fig. S4. Ultrastructural features of mock infected cells of an *in vitro* model of blood-brain endothelial barrier.

Low-magnification transmission electron micrograph of 7-day hCMEC/D3 monolayers (a and b). Confocal observation of mitochondria network (red) in hCMEC/D3 cells (c), High magnification transmission electron micrograph of 7-days cultures hCMEC/D3 monolayer. A central nucleus is surrounded by plenty of mitochondria near the rough endoplasmic reticulum (d). Bars represent, 10 µm (a – c); 5 µm (d). N, nucleus; M, mitochondria; ER, endoplasmic reticulum.

General features of Enterovirus strains			Clinical features	
Species	**Serotypes**	**Strains**	**Isolation source**	**Clinical manifestations**
	CV-A2	CF192073-11	Throat	Encephalitis
		CF197013-11	Feces	Guillain Barre
	CV-A4	CF308011-10	Throat	Hand-Foot and Mouth disease
		CF063006-11	Feces	Fever
A	CV-A5	CF193056-11	Feces	Acute meningitis
	CV-A6	CF218013-10	Throat	Hand-Foot and Mouth disease
		CF605-00	Feces	Septic shock
	EV-A71	CF166105-10	Throat	Hand-Foot and Mouth disease
		CF160019-10	Throat	Hand-Foot and Mouth disease
	CV-A9	CF027040-07	Throat	Acute meningitis
	CV-B1	CF741-93	Feces	
		CF217010-08	Feces	
	CV-B2	CF314051-04	Throat	
		CF186019-07	Throat	Acute meningitis
		NANCY	Stools	Minor febril illness
	CV-B3	CF183076-08	Throat	Acute meningitis
		CF193061-05	Throat	Acute meningitis
	CV-B4	CF169091-07	Throat	Acute meningitis
		CF516-00	CSF	Headache; Fever; Vomiting
	CV-B5	CF186106-05	Throat	Acute meningitis
		CF202076-06	Throat	Acute meningitis
	CV-B6	**SCHMITT**	Stools	None
		CF132-87		
	E1	**FAROUK**	Stools	None
	E2	**CORNELIS**	Stools	Acute meningitis
		CF307001-05	Feces	Acute meningitis suspected
	E3	**MORRISSEY**	Stools	Acute meningitis
		CF180108-05	Throat	
		DUTOIT		
	E4	CF248076-05	Feces	
		CF101013-08	Feces	Acute meningitis
	E5	**NOYCE**	Stools	Acute meningitis
		CF990-00	CSF	Acute meningitis
		CF2660-01	CSF	Acute meningitis
		CF1057-00	CSF	Acute meningitis
		CF328087-03	Throat	Acute meningitis
	E6	CF671-00	CSF	Acute meningitis
		CF1634-01	CSF	Acute meningitis
		CF1679-02	CSF	Acute meningitis
		CF158061-11	Throat	
		CF185010-11	Throat	Acute meningitis
	E7	**WALLACE**	Stools	None
		CF185103-05	Throat	Acute meningitis
	E9	CF293042-06	Throat	Acute meningitis
		CF22-80		
	E11	CF1462-00	CSF	Acute meningitis
		CF228046-07	Throat	Acute meningitis suspected
B	E12	CF1157-91		
		DELCARMEN	Stools	None
		CF1083-91		
		CF1274-00	CSF	Acute meningitis
	E13	CF1925-01	CSF	Acute meningitis
		CF1393-00	CSF	Acute meningitis
		CF1901-00	Throat	Acute meningitis
		CF282003-06	Throat	Acute meningitis
	E14	**TOW**	Stools	Acute meningitis
		CF225059-08	Feces	
	E15	**CHARLESTON**	Stools	None
	E16	CF187056-09	Feces	Acute meningitis
	E17	CF596-78		
		METCALF	Stools	Diarrhea
	E18	CF279084-05	Throat	Acute meningitis
		TR115015-05		
	E19	**BURKE**	Stools	Diarrhea
	E20	**JV1**	Stools	Fever
	E21	**FARINA**	Stools	Acute meningitis
	E24	**DECAMP**	Stools	Diarrhea
		JV4	Stools	Diarrhea
	E25	CF205083-06	Throat	Acute meningitis
		CF199022-07	Feces	Acute meningitis
	E26	**CORONEL**	Stools	None
	E27	**BACON**	Stools	None
	E29	**JV10**	Stools	None
		BASTIANNI	CSF	Acute meningitis
		CF1260-78		
		CF1074-78		
		CF282-97	Feces	Acute meningitis
	E30	CF552-00	Feces	Acute meningitis
		CF2575-00	CSF	Acute meningitis
		CF220062-05	Throat	Acute meningitis
		CF307026-07	Throat	Acute meningitis
		CF284052-07	Throat	Acute meningitis
	E31	**CALDWELL**	Stools	Acute meningitis
	E33	CF235069-05	Throat	Acute meningitis
	EV-B69	**TOLUCA1**	Rectal swab	None
	EV-B77	CF496-99	Feces	
C	CV-A21	CF1069-91		
D	EV-D70	CF670-71		